LAWRENCE
LIVERMORE
NATIONAL
LABORATORY

LLNL-PROC-420584

High Performance Capsule Implosions on the OMEGA Laser Facility with Rugby Hohlraums

H. F. Robey, P. Amendt, H. Park, R. Town, J. L. Milovich, T. Doeppner, D. E. Hinkel, R. Wallace, C. Sorce, F. Philippe, A. Casner, T. Caillaud, O. Landoas, S. Liberatore, S. Laffitt, M. Monteil, F. Sequin, M. Rosenberg, C. K. Li, R. Petrasso, V. Glebov, C. Stoekl, A. Nikroo, E. Giraldez

November 23, 2009

51st Annual Meeting of the APS Division of Plasma Physics
Atlanta, GA, United States
November 1, 2009 through November 6, 2009

Disclaimer

Manuscript for submission to *Physics of Plasmas*

High Performance Capsule Implosions on the OMEGA Laser Facility with Rugby Hohlraums*

H. F. Robey, P. Amendt, H.-S. Park, R. Town, J. L. Milovich, T. Doeppner,
D. E. Hinkel, R. Wallace, C. Sorce
[1]Lawrence Livermore National Laboratory, Livermore, CA

F. Philippe, A. Casner, T. Caillaud, O. Landoas, S. Liberatore, S. Laffitt, M.-C. Monteil,
CEA, DAM, DIF, F-91297 Arpajon, France

F. Sequin, M. Rosenberg, C.K. Li, and R. Petrasso
Plasma Science and Fusion Center, Massachusetts Institute of Technology, Cambridge, Massachusetts

V. Glebov, C. Stoekl
Laboratory for Laser Energetics, University of Rochester, Rochester, New York

A. Nikroo, E. Giraldez
General Atomics, San Diego, CA

ABSTRACT

Rugby-shaped hohlraums have been proposed [1] as a method for x-ray drive enhancement for indirectly-driven capsule implosions. This concept has recently been tested in a series of shots on the OMEGA laser facility at the Laboratory for Laser Energetics at the University of Rochester. In this paper, experimental results are presented comparing the performance of D_2-filled capsules between standard cylindrical Au hohlraums and rugby-shaped hohlraums. The rugby hohlraums demonstrated 18% more x-ray drive energy as compared with the cylinders, and the high-performance

design of these implosions (both cylinder and rugby) also provided ≈ 20x more deuterium (DD) neutrons than any previous indirectly-driven campaign on Omega (and ≈ 3x more than ever achieved on NOVA implosions driven with nearly twice the laser energy). This increase in performance enables, for the first time, a measurement of the neutron burn history and imaging of the neutron core shapes in an indirectly-driven implosion. Previous DD neutron yields had been too low to register this key measurement of capsule performance and the effects of dynamic mix. A wealth of additional data on the fuel areal density from the suite of charged particle diagnostics was obtained on a subset of the shots that used D^3He rather than D_2 fuel. Comparisons of the experimental results with numerical simulations are shown to be in very good agreement. The design techniques employed in this campaign, e.g., smaller NIF-like laser entrance holes and hohlraum case-to-capsule ratios, provide added confidence in the pursuit of ignition on the National Ignition Facility [2].

I. INTRODUCTION

In the indirect-drive approach to inertial confinement fusion (ICF), a high-Z radiation enclosure (or hohlraum) is used to convert incident laser light into x rays to uniformly irradiate a capsule place at the hohlraum center. The vast majority of previous experiments have employed hohlraums of cylindrical shape [3-5]. Recently, there has been increasing interest in hohlraums of an elliptical or "rugby" shape [6-10], as this design provides the possibility of reduced energy losses into the wall and therefore enhanced radiation drive for a given laser energy input. These hohlraums are currently being investigated for a number of inertial confinement fusion applications. Early experiments on the Laser MegaJoule (LMJ) [11], for example, will use a two laser-cone irradiation scheme (per side), for which a rugby hohlraum shape has several advantages [6, 7]. Rugby hohlraums have also been proposed for the implosion of a double-shell capsule on the National Ignition Facility (NIF) [10], and they are also being considered for the Laser Inertial Fusion Energy (LIFE) program [12].

The advantage of the rugby hohlraum shape can be easily seen by considering an energy balance in the hohlraum. Following Lindl [2], we can write down the energy balance between sources and sinks as

$$\eta_{ce} \cdot E_{laser} = E_{wall} + E_{LEH} + E_{capsule} = f(T_R^4,\ A_{wall},\ A_{LEH},\ A_{capsule},\ \tau) \qquad (1)$$

where E_{laser} is the incident laser energy, E_{wall} is the energy lost to the hohlraum wall with area A_{wall}, E_{LEH} is the energy lost out of the laser entrance holes (LEH), and $E_{capsule}$ is the energy absorbed by the capsule. Here, η_{ce} is the conversion efficiency from laser energy to x rays, and T_R is the steady-state radiation temperature attained for a constant power laser pulse of duration τ. As an example, consider the comparison of hohlraum shapes shown in Figure 1, which compares a cylinder and a rugby with the same equatorial and LEH diameters. As a specific example, let's consider the dimensions of the design presented in [10]. The areas of the wall, capsule, and LEH are summarized in Table I.

Table I.

	Rugby	Cylinder
Hohlraum length (μm)	2275	2450
Hohlraum radius (μm)	800	800
LEH	50%	50%
Hohlraum corner radius (μm)	800	150
Area LEH (x2) (mm^2)	1.0	1.0
Area capsule (mm^2)	0.67	0.67
Area wall (mm^2)	9.6	13.9

The peak T_R obtained from eqn. (1) in the rugby is predicted to be 245 eV vs. a peak of only 229 eV for the cylinder. This corresponds to a 31% increase in the radiation flux between the two hohlraums.

There is clearly a significant additional energy loss to the wall in the corners of the cylindrical hohlraum. The corner radius of the cylinder used in this estimate is that of an Omega "scale-1" hohlraum, $r_{corner} = 150\mu$m, which is 19% of the hohlraum radius at the

equator. The corresponding ratio in the rugby, by comparison, is 1.0, as the wall contour is by definition [1] an arc of a circle. It is interesting to compare these relative corner radii with those of a candidate NIF ignition hohlraum with corner and hohlraum radii of 1.2 and 2.72 mm, respectively (giving a ratio of 0.44) [13]. Increasing the corner radius of the Omega-scale cylinder of Figure 1 to 44% of the hohlraum radius (r_{corner} = 352 μm) raises the peak T_R to 235 eV, which is still 19% lower flux than the rugby design. The NIF design therefore falls in between the two cases considered here with a smaller relative energy loss in the corners than the Omega-scale cylinder but a greater relative energy loss than in a rugby design.

Recently, a numerical design study comparing the performance of traditional cylindrical vs. rugby hohlraums was presented [10]. In this study, a high performance implosion design was presented, which predicted a substantial increase in drive in the rugby hohlraum. The performance predictions of [10] were recently tested in a series of experiments on the OMEGA Laser Facility [14] at the Laboratory for Laser Energetics (LLE), University of Rochester. Details of the experiment and an overview of the experimental results have been recently reported in [8, 9]. The goal of these experiments was two-fold. First, the high-performance design promised a sufficient increase in the neutron yield to access additional neutron diagnostics, which heretofore have not been accessible using indirect drive. Second, these experiments were the first direct comparison of cylindrical vs. rugby hohlraums and provide an opportunity to demonstrate the predicted drive advantage of rugby hohlraums.

Both of these goals were successfully met. As reported in [9], record indirectly-driven DD neutron yields in excess of 10^{10} were achieved, in agreement with pre-shot simulations [10]. This yield increase enabled the first demonstration of both a neutron imaging system (NIS) developed by the CEA [15] and the LLE neutron temporal diagnostic (NTD) [16, 17], which provides a temporal history of the neutron production. In this paper, the results of these experiments are presented together with comparisons with post-shot numerical simulations.

II. EXPERIMENTAL PARAMETERS

Figure 2 shows photographs of the targets used in the experiments. The axial view shown on the left is essentially identical for both hohlraums. The diameters of the equator, the LEH, and the capsule are the same for both hohlraums. The side view shows the tapered wall of the rugby hohlraum. The square feature seen in the center of both side-views is a thin CH patch over-coated with 2 μm of Au. This patch covers a 300 μm diameter diagnostic hole to enable viewing of the x-ray emission from the imploded core of the capsule.

The capsule shells used in these experiments consisted of a 9.8 μm thick CH (polystyrene) mandrel, a 2.6 μm thick polyvinylacetate (PVA) layer, and a 2.7% Ge-doped CH layer of variable thickness. Table II summarizes the hohlraum type, capsule inside diameter (ID), outside diameter (OD), Ge-doped layer thickness, total wall thickness, gas-fill species, and gas-fill pressure for each capsule.

Table II. Capsule Parameters

Shot	54734	54735	54736	54738	54739	54740	54741	54744	54745	54746	54747	54748
hohlraum	rugby	rugby	rugby	rugby	rugby	rugby	rugby	cyl	cyl	cyl	cyl	cyl
OD (μm)	643.4	650.4	654.2	650.8	650.6	655.8	664.8	647.4	668.4	645.4	657.4	647.0
ID (μm)	548	553	561	559	555	549	556	551	566	553	567	550
Ge-layer	35.3	36.3	34.2	33.5	35.4	41	42	35.8	38.8	33.8	32.8	36.1
Total wall	47.7	48.7	46.6	45.9	47.8	53.4	54.4	48.2	51.2	46.2	45.2	48.5
Gas	DD	DD	DD	DD	D^3He	D^3He	D^3He	D^3He	D^3He	DD	DD	DD
Pr (atm)	10	10	50	50	50	50	50	50	50	50	50	50

Seven of the capsules used pure deuterium (D2) fuel at fill pressures of 50 atm and 10 atm to test the role of convergence and increasing effects of interfacial mixing. The remaining 5 capsules used D^3He fuel to access the suite of charged particle diagnostics.

The hohlraums were all driven with 40 beams of Omega with 20 beams directed into each LEH. The total laser energy on target was very repeatable from shot-to-shot with an average laser energy of 19.62 ± 0.17 kJ. Distributed phase plates of elliptical shape (E-IDI-300) [18] with a nominal 300 μm spot width were used for beam smoothing. No smoothing by spectral dispersion (SSD) [19] or polarization smoothing using distributed polarization rotators (DPR) [20] were used in order to maximize the laser energy

delivered to the hohlraum. Figure 3 shows the nominal pointing of the three cones of beams at angles of 23.2° (cone 1), 42° (cone 2), and 58.9° (cone 3) in the two hohlraums. The beam pointing and defocus values, relative to the center of each LEH, are identical. Since the rugby hohlraum is 175 μm shorter in length than the cylinder, the cone 1 beams pass the capsule in slightly closer proximity than in the cylinder. An important difference is noted in the cone 3 beams as well. Due to the tapered shape of the rugby wall near the LEH, the cone 3 beams intercept the wall at an axial position closer to the LEH than in the cylinder. Note also that the cone 3 beam spots on the hohlraum wall in the rugby are considerably larger than in the cylinder. These beams will therefore pass through a longer path length of ablated Au plasma than in the cylinder. This will be of importance when we consider the backscatter data in Section IV.

III. EXPERIMENTAL CONFIRMATION OF RUGBY DRIVE ENHANCEMENT

In [9], an extensive summary and discussion of the neutron yields from these experiments was presented. We will not further elaborate on these results except to reiterate that the design of these implosions did indeed result in the highest yield ever reported in an indirectly-driven implosion with D2 fuel. The yields of both the rugby ($1.29\text{x}10^{10}$ and $1.51\text{x}10^{10}$) and cylinder ($1.22\text{x}10^{10}$ and $1.37\text{x}10^{10}$) were approximately 20 times greater than the previous Omega record of $8\text{x}10^{10}$ and 3X greater than the Nova record of $4\text{x}10^{9}$, which was achieved with 32 kJ of laser energy input as compared to the 19.5 kJ used in these experiments. We note also that the measure yields showed relatively little difference between rugby and cylinders as predicted [1]. It is important to note, however, that the symmetry and capsule thickness tuning was considerably better in the cylinders, as will be demonstrated.

We now turn our attention to the drive advantage of rugby hohlraums. Figure 4(a) shows the full radiation drive history (0 to 2 keV) as measured by Dante [21] for all of the shots. Figure 4(b) gives the details near the time of peak x-ray drive. As can be seen, the repeatability of the data is very good and clearly demonstrates a consistent 10 eV increase in the rugby hohlraums. Comparing this peak drive with the energetics estimates presented in Section I, we see that the peak T_R in the cylinders is very close to

that predicted, whereas the peak T_R in the rugby is about 5 eV lower than that predicted by the energy balance. If we include a 10% backscattered energy loss in the rugby hohlraum, this brings the energetics estimate into agreement with the measurements. In Section IV, it will be shown that this estimate is consistent with observations from a wide range of additional diagnostics of the implosion performance.

A very important (and independent, target-center based) confirmation of this drive increase is obtained from the charged particle diagnostics. Two types of charged particle diagnostics were used on this shots, with up to three fielded from different viewing angles on a single shot. Spatially resolving CR39 nuclear track detectors [22] were used to obtain images of the proton fluence, and spectrally-resolving wedge range filters (WRF) [22] were used to obtain spectra of the downscattered protons vs. position. The CR39 measurements, which are extensively discussed in [23], showed considerable anisotropy when viewed through the LEH, but were reasonably isotropic when viewed from the equator. For this reason, we will focus on results obtained from diagnostic orientations viewing the equator. The WRFs record the spectrum of protons originating from the reaction of D + ^{3}He -> p(14.7 MeV) + α(3.6 MeV) and characteristically show protons generated in two episodes, one at shock convergence at the origin (shock flash) and one at peak compression. Figure 5(a) shows a typical example of the downscattered spectrum. The shock flash peak at about 13 MeV is due to protons generated at shock stagnation (when the fuel and capsule areal density is still low), and the broader peak centered at 11 MeV is due to the downshift of protons generated at peak compression, which traverse higher capsule areal density. Figure 5(b) compares the energy downshift, corrected for the energy loss of the protons passing through the 25μm Au hohlraum wall, for both rugby and cylinder at several viewing orientations. Several observations can be made. First, we note that the variation as a function of position from equator to pole and back to equator is reasonably uniform. Second, the shock-flash generated protons show very little variation between the two hohlraums. This occurs because the shock flash occurs prior to any significant shell convergence, at which time the capsules in the rugby and cylinder have very similar areal densities.

We now compare the results for the compressional down shift in the cylindrical hohlraums. The downshift increases with increasing areal density ρR as can be seen for

the two initial ablator thicknesses shown for the cylinders. An increase of 3 μm in the initial ablator thickness corresponds to an additional 0.4 MeV increase in the proton energy downshift. Next we compare the results for the 48.2 μm thick ablator in a cylinder with a very similar 47.8 μm thick ablator in a rugby hohlraums. The measured energy downshift in the rugby is 0.8 MeV lower than the results for the cylinder with comparable ablator thickness. Based on the observation from the cylinders, this implies an additional 6 μm of ablated mass in the rugby hohlraum. This increase in mass ablation in the rugby hohlraums serves as a capsule-centric confirmation of the enhanced drive.

IV. ADDITIONAL EXPERIMENTAL OBSERVATIONS

A number of additional diagnostics were used on these shots as well, and while all returned high quality data, several observations were not in agreement with pre-shot simulations. Figure 6, for example, gives a summary of the measured neutron bang times for each of the shots. The error bars on the data are ±50 ps from the shots where good NTD data were obtained, and ±100 ps on shots where the bang time is measured with the less sensitive NBT detector [24]. From pre-shot simulations [1], it was expected that the x-ray bang times in the rugby hohlraums would be earlier by about 200 ps than in the cylinders due to the increase in drive. For the 50 atm DD capsules, for example, the bang time was predicted to be 1.7 ns in rugby hohlraums vs. 1.9 ns in cylinders. Including information about the as-shot capsule thicknesses, the bang times for the cylinders are in reasonable agreement with pre-shot simulations, while those for the rugby hohlraums are consistently late.

X-ray core emission images were obtained on all of the shots providing information about the implosion symmetry. Figure 7(a) shows images of the core emission from both D2-filled and D^3He-filled capsules in the two hohlraums. The emission was recorded with a gated x-ray framing camera [25] through a 300 μm diagnostic hole in the side of the hohlraum. The hole was covered with a 20 μm CH patch over-coated with 2 μm of Au on the interior side to maintain the hohlraum albedo. The images shown in Figure 7(a) are 230 x 230 μm in extent, and in all cases the hohlraum axis is vertical. The examples of Figure 7(a) are fully representative of all shots, where the implosion core

shapes were consistently more "pancaked" (or oblate) in the rugby hohlraums. Figure 7(b) quantifies the core symmetry by plotting the normalized Legendre polynomial coefficient P_2 / P_0 extracted from an analysis of the 50% emission contour taken at the time of peak x-ray emission. For each hohlraum type, the Legendre mode coefficient is shown for a 10 atm D2, a 50 atm D2, and a 50 atm D^3He-filled capsule. The symmetry is very good for all implosions in cylinders and consistently pancaked in all of the rugbys with P_2 / P_0 = -20 to -28%.

The reason for the change in symmetry becomes apparent when one looks at the data from the backscatter diagnostics. Figure 8 shows the data from the Full Aperture Backscatter Station (FABS) diagnostic [26], which was fielded on one of the cone 3 beams (#25). The location of beam 25 on the hohlraum wall is shown in the inset for each case. In all shots, backscattered energy from stimulated Brillouin scattering (SBS) was observed, whereas no measurable stimulated Raman Scattering (SRS) was seen on any of the shots. In addition, the Near Backscatter Imager (NBI) diagnostic [27] was fielded, but in all cases less than 10% additional energy above that seen by the FABS was recorded. Figure 8(a) shows that the backscattered energy was very consistent within shots with a given hohlraum shape. The average backscattered energy was 7.2% in the rugby hohlraums and 1.3% in the cylinders. The variation within the rugby hohlraums is even more consistent, when one notes that the first shot had a slightly different focus location for the cone 1 and cone 3 beams than the remaining 6 shots. Between shots 1 and 2, the focus of cone 1 was moved from the center of the LEH to a position 400 μm inside the LEH. The focus of the cone 3 beams was also moved inward from 1450 μm to 650 μm outside of the LEH. This change in beam focus toward the hohlraum interior was made after observation of the core symmetry in the first shot, where it was suspected that the beams were possibly clipping on the rather small LEH opening. This focal change caused a very consistent 10% increase in the backscatter level.

Figure 8(b) shows the corresponding backscattered power history comparison between a rugby and cylindrical hohlraum. In both cases, the backscatter is observed early in the pulse. For the rugby, it is significant for the first 600 ps of the pulse, and negligible thereafter.

A related measurement is obtained from the Hard X-Ray Detector (HXRD) [28], which is a strongly filtered four-channel array of x-ray diodes recording hohlraum emission of x-ray photons above 20, 40, 60, and 80 keV, respectively. For the present series of shots, only two channels (1 and 4) of this detector were operational. Figure 9 shows a comparison of the 80 keV channel response for a rugby and a cylinder. The absolute time reference on this plot is arbitrary, as the detector timing was not calibrated for these shots. The hard x-ray signal is approximately 20 times greater in the rugby, indicating that there is likely considerable SRS occurring on the inner cones, which were not measured with the FABS or NBI due to the hohlraum orientation. This observation is consistent with previous measurements in an empty (no capsule) vacuum rugby-like hohlraum experiment reported recently by Casner *et al*. [7]. Though the hohlraum shape and beam pointing were slightly different in that experiment, the backscatter was measured to be 5% on cone 2 and 10% (with 5% SRS) on cone 1. No directly comparable results for a cylindrical hohlraum were obtained in those experiments, however. To fully characterize the backscatter difference between a rugby and cylindrical hohlraum, a dedicated measurement of the inner cone backscatter would be needed.

V. COMPARISON WITH NUMERICAL SIMULATION

To briefly summarize the observations in Sections III and IV, two of the diagnostics gave a clear signature of drive enhancement in rugby hohlraums. (1) An external measurement of the hohlraum radiation flux (Dante) showed a very repeatable 10 eV increase in the peak flux, and (2) a measurement of the energy downshift of 14.7 MeV protons produced at the capsule center demonstrated smaller energy downshifts consistent with enhanced mass ablation in the rugby hohlraum. Several other diagnostics, however, gave results which were not expected from pre-shot predictions: (1) backscatter was significantly higher in the rugby hohlraums, (2) x-ray core emission in rugby hohlraums was less symmetric than cylinders, and (3) x-ray bang times in rugby hohlraums were later than expected. In order to explore this, post-shot simulations have been performed. These simulations include measured laser power histories and as-shot

capsule diameters, wall thicknesses, and dopant concentrations. The measured time-dependent outer-cone backscatter is used, and a range of assumed inner-cone backscatter levels is included to assess the effect on all diagnostics.

Table III gives a summary of the post-shot simulated yields for both hohlraums. For the cylinder, simulations are performed with (1) no backscatter, (2) the inclusion of the measured cone 3 backscatter, and (3) an additional 1.3% backscatter on both inner cones with the same measured time dependence as for cone 3. As Table III shows, for these small levels of backscatter, there is little variation in the simulated yields, and the ratio of the measured yield over the simulated clean (i.e., no mix) yield ("YOC") is always over 80%, indicating excellent agreement. For the rugby, simulations are again performed with no backscatter, measured outer cone backscatter, and a range of inner cone values from 5 to 20%, all with the same time dependence as that measured for cone 3. From Table III, the simulated yield falls with increasing backscatter, and the YOC increases from 48 to 62%, all in very reasonable agreement with the data.

Table III

Rugby Backscatter	Rugby yield	Rugby YOC (%)	Cylinder backscatter	Cylinder Yield	Cylinder YOC
None	$2.70\ 10^{10}$	48	None	$1.64\ 10^{10}$	83
7.2%, cone 3	$2.57\ 10^{10}$	50	1.3%, cone 3	$1.57\ 10^{10}$	87
+ 5% cones 1 & 2	$2.50\ 10^{10}$	52	+1.3% cones 1 & 2	$1.50\ 10^{10}$	91
+10% cones 1 & 3	$2.33\ 10^{10}$	55			
+15% cones 1 & 3	$2.15\ 10^{10}$	60			
+20% cones 1 &3	$2.07\ 10^{10}$	62			

Turning now to the drive comparison, Figure 10(a) shows a comparison of the measured Dante for a 50 atm D2 rugby shot (#54736) with the simulated Dante histories for the assumed range of inner cone backscatter. As is seen, due to the time dependence of the backscatter, the simulated drive is most strongly affected in the first half of the pulse. The simulations with at least 10% assumed backscatter on the inner cones are within the ±5% error bars on the Dante data throughout the pulse. The discrepancy

between data and simulation for t > 1.5 ns is due to incorrect modeling of LEH closure in the simulations, but occurs too late to have any impact on any of the simulated observables.

Figure 10(b) shows a comparison of the simulated drive between the rugby and the cylinder. The red curves are for the rugby hohlraum, and the black curves are for the cylinder. Dashed curves give the simulated Dante in the absence of backscatter, and solid curves give the result with 15% and 1.3% assumed inner-cone backscatter in the rugby and cylinder, respectively. As is seen, there is very little change in the cylinder due to the very small level of the backscatter correction. For the rugby, however, inclusion of backscatter significantly decreases the drive early in time while still achieving a peak T_R that is 7 eV higher that that in the cylinder. This time-dependent drive difference is important, as it explains the bang-time discrepancy noted earlier in Section IV.

Figure 11 shows the comparison between the simulated x-ray bang times and the post-shot simulations. The simulation with no backscatter (red symbol) is early by nearly 200 ps as compared to the data for shot #54736, where we have included the more stringent ± 50 ps error bars from the NTD measurement. With increasing assumed backscatter (blue symbols) and correspondingly reduced drive, the simulated x-ray bang time is increasingly delayed. The simulations with inner cone backscatter levels of 15 - 20% fall within the error bars of the data. This is consistent with the value of >10% that provided agreement between the simulated drive and the Dante data of Figure 10. The previous observation from Figure 6 that bang times were similar in rugby and cylindrical hohlraums can now be understood: Inclusion of backscatter losses in a rugby decreases the drive early, but still achieves a higher peak flux, resulting in similar bang times.

An assumption of 15% inner cone backscatter is consistent with the x-ray core emission images as well. Figures 12(a-f) show simulated emission images for the range of assumed backscatter on the inner cones. Legendre polynomial coefficients, again extracted from the 50% contour levels, are shown in Figure 12(g). As before, the simulation with no backscatter is shown with the red symbol, simulation results with assumed inner cone backscatter are shown with blue symbols, and the data with ±5% error bars is shown in green. The simulation with 15% assumed inner-cone backscatter

falls right in the middle of the error bars of the data, further supporting the agreement seen in the Dante and x-ray bang-time comparisons.

Figure 13 show a comparison of the simulated proton spectra vs. the assumed level of inner cone backscatter. Spectra are shown at both the pole (black) and the equator (red). A number of interesting effects are observed in the simulated proton spectra with increasing backscatter. As Figure 13 shows, the total proton yield decreases as a result of the decreased drive, ranging from 3.4 x 10^7 with no backscatter to 1.3 x 10^7 with 20% assumed backscatter. Also, the shock-flash-generated protons are observed to decrease at a faster rate than those created at compression. This is due to the very strong temperature dependence of the shock-generated protons, and the decrease in this temperature as the symmetry of the implosion is changed with increasing backscatter on the inner cones. The proton energy downshift of the compressional peak increases with the decrease in drive, as more mass remains at bang time with the reduced drive. With no backscatter, the compressional protons are downshifted with a spectral peak at 13.4 MeV, while the simulation with 20% assumed inner cone backscatter shows a peak of the compressional protons at 12.7 MeV.

Figure 14 quantifies the comparison of the simulated proton spectra with the data of Figure 5. Figure 14(a) plots the simulated energy downshift for the shock-generated protons (green symbols), the compressional protons in rugby hohlraums (blue), and a single point (red star) for the compressional protons in a cylindrical hohlraum. As with the other diagnostics, the simulation with 15% assumed inner cone backscatter is in excellent agreement with the data (shot #54739), where the error bars are taken from the observed angular variation in the data between the two equatorial measurements. The comparison between simulation and the data is shown in Figure 14(b), where both compressional and shock-flash generated energy downshifts are in excellent agreement with the data for both hohlraums.

VI. SUMMARY AND DIRECTIONS FOR FUTURE WORK

In summary, the first direct comparison of the performance of rugby vs. cylindrical hohlraums has been presented. The performance of both with regard to neutron yield was

excellent due to the more NIF-like (i.e., smaller LEH diameters and smaller case-to-capsule ratios), high-performance design of the implosions. Record DD neutron yields were obtained in both cases. The rugby hohlraums demonstrated 18% more x-ray drive energy as compared with the cylinders. This drive enhancement was verified both by an external measurement of the hohlraum x-ray radiation flux (Dante) as well as by an internal capsule-centric measurement of the energy downshift of protons in D^3He-filled capsules.

SBS backscatter was observed to be significantly higher in the rugby hohlraums. This affected the implosion symmetry, the measured x-ray bang times, and the energy downshift in the proton spectra in the rugby hohlraums. Post-shot numerical simulations that include an assumed 15% energy loss on the inner cones due to backscatter were found to be in very good agreement with all observations.

Future work with rugby hohlraums needs to address the relatively higher backscatter, which partially offsets the drive enhancement. A number of techniques can be investigated to reduce the level of backscatter. Beam smoothing either by spectral dispersion or polarization rotation can be implemented, Boron-doping of the Au walls has been suggested to suppress SBS in NIF hohlraums [29], and gas-fill in the hohlraum would reduce the extent of the ablated Au plasma. Additional experiments on Omega can be used to assess many of these issues, but to assess the full potential of the rugby geometry experiments on a mega-joule class laser such as NIF or LMJ will be required.

VII. ACKNOWLEDGEMENTS

This work was performed under the auspices of the DOE by Lawrence Livermore National Laboratory under Contract DE-AC52-07NA27344.

VIII. REFERENCES

[1] P. Amendt, C. Cerjan, A. Hamza, D. E. Hinkel, J. L.Milovich, H.-S. Park, and H. F. Robey, *Phys. Plasmas* **15**, 012702 (2008).

[2] J. D. Lindl, P. Amendt, R. L. Berger, S. G. Glendinning, S. H. Glenzer, S. W. Haan, R. L. Kauffman, O. L. Landen, and L. J. Suter, *Phys. Plasmas* **11**, 339 (2004).

[3] J. Schein, O. Jones, M. Rosen, E. Dewald, S. Glenzer, J. Gunther, B. Hammel, O. Landen, L. Suter, and R. Wallace, *Phys. Rev. Lett.* **98**, 175003 (2007).

[4] P. E. Young, M. D. Rosen, J. H. Hammer, W. S. Hsing, S. G. Glendinning, R. E.Turner, R. Kirkwood, J. Schein, C. Sorce, J. J. H. Satcher et al, *Phys. Rev. Lett.* **101**, 035001 (2008).

[5] D. A. Callahan, P. A. Amendt, E. L. Dewald, S. W. Haan, D. E. Hinkel, N. Izumi, O. S. Jones, O. L. Landen, J. D. Lindl, S. M. Pollaine, et al., *Phys. Plasmas* **13**, 056307 (2006).

[6] M. Vandenboomgaerde, J. Bastian, A. Casner, D. Galmiche, J.-P. Jadaud, S. Laffite, S. Liberatore, G. Malinie, and F. Philippe, *Phys. Rev. Lett.* **99** 065004 (2007).

[7] A. Casner, D. Galmiche, G. Huser, J.-P. Jadaud , S. Liberatore, and M. Vandenboomgaerde, *Phys. Plasmas* **16**, 092701 (2009).

[8] F. Phillippe *et al*., Proc. IFSA (2009).

[9] F. Phillipe, A. Casner, T. Caillaud, O. Landoas, M. C. Monteil, S. Liberatore, H.-S. Park, P. Amendt, H. F. Robey, C. Sorce, C. K. Li, F. Seguin, M. Rosenberg, R. Petrasso, V. Glebov, and C. Stoekl, submitted to *Phys. Rev. Lett.* (2009).

[10] P. Amendt, C. Cerjan, A. Hamza, D. E. Hinkel, J. L.Milovich, and H. F. Robey, *Phys. Plasmas* **14**, 056312 (2007).

[11] C. Cavailler, *Plamsa Phys. Control. Fusion* **47**, 389 (2005).

[12] E. I. Moses, *Fus. Sci. Technol.* **56**, 547 (2009).

[13] S. W. Haan, Table of Requirements for NIF Ignition Point Design and Alternates, Version Rev. 3.11, private communication (2008).

[14] T. R. Boehly, D. L. Brown, R. S. Craxton, R. L. Keck, J. P. Knauer, J. H. Kelly, T. J. Kessler, S. A. Kumpan, S. J. Loucks, S. A. Letzring, F. J. Marshall, R. L. McCrory, S. F. B. Morse, W. Seka, J. M. Soures, C. P. Verdon, *Opt. Commun.* **133**, 495 (1997).

[15] T. Caillaud, O. Landoas, I. Thfoin, B. Rosse, M. Briat, L. Disdier, F. Phillipe, A. Casner, J. L. Bourgade, V. Yu. Glebov, F. J. Marshall, T. C. Sangster, H.-S. Park, H. F. Robey, P. Amendt, *Bull. Am. Phys. Soc.,* **54** (15), T07.00004 (2009).

[16] R. A. Lerche D. W. Phillion, and G. L. Tietbohl, *et al*., *Rev. Sci. Instrum.* **66**, 933 (1995).

[17] C. Stoekl *et al*., *Rev. Sci. Instrum.* **73**, 3796 (2002).

[18] S. Regan *et al*., *J. Phys. Conf. Ser.* **17**, 022077 (2008).

[19] Laboratory for Laser Energetics LLE Review **80**, 197, NTIS document No. DOE/SF/19460-321 (1999). Copies may be obtained from the National Technical Information Service, Springfield, VA 22161.

[20] Laboratory for Laser Energetics LLE Review **45**, 1, NTIS document No. DOE/ DP40200-149 (1990). Copies may be obtained from the National Technical Information Service, Springfield, VA 22161.

[21] C. Sorce, J. Schein, F. Weber, K. Widmann, K. Campbell, E. Dewald, R. Turner, and O. Landen, *Rev. Sci. Instrum.* **77**, 10E518 (2006).
[22] F. H. Seguin, J. A. Frenje, C. K. Li, D. G. Hicks, S. Kurebayashi, J. R. Rygg, B.-E. Schwartz, R. D. Petrasso, S. Roberts, J. M. Soures, D. D. Meyerhofer, T. C. Sangster, J. P. Knauer, C. Sorce, V. Y. Glebov, C. Stoekl, T. W. Phillips, R. J. Leeper, K. Fletcher, and S. Padalino, *Rev. Sci. Instrum.* **74** (2), 975 (2003).
[23] R. Petrasso, C. Li, F. Seguin, J. Frenje, M. Rosenberg, H. Rinderknecht, F. Phillipe, A. Casner, T. Caillaud, O. Landoas, J.-L Bourgade, P. Amendt, N. Izumi, J. Koch, O. Landen, J. Milovich, H. Park, H. Robey, R. Robey, R. Town, A. Nikroo, J. Kilkenny, *Bull. Am. Phys. Soc.*, **54** (15), B05.00012 (2009).; C. K. Li *et. al.*, in preparation for *Phys. Rev. Lett.*
[24] University of Rochester LLE Review Quarterly Report **88**, 171 (2001).
[25] K. S. Budil, T. S. Perry, P. M. Bell, J. D. Hares, P. L. Miller, T. A. Peyser, R. Wallace, H. Louis, D. E. Smith, *Rev. Sci. Instrum.* **67**, 485 (1996).
[26] S. Regan et al., *Phys. Plasmas* **6**, 2072 (1999).
[27] P. Neumayer et al., *Rev. Sci. Instrum.* **79**, 10F548 (2008).
[28] C. Stoeckl et al., *Rev. Sci. Instrum.* **72**, 1197 (2001).
[29] N. Meezan et al., *J. Phys. Conf. Ser.* **112** (2008).

IX. TABLES

[1] Comparison of capsule, wall, and LEH dimensions for a cylinder vs rugby hohlraum

[2] Summary of capsule parameters

[3] Comparison of simulated yields and yield-over-clean (YOC) for rugby vs. cylindrical hohlraums

X. FIGURE CAPTIONS

[1] Schematic drawing comparing the relative dimensions of a rugby and cylindrical hohlraum

[2] Photographs of the targets, axial and side views

[3] Schematic drawing showing the pointing of the three beam cones in rugby vs. cylindrical hohlraums

[4] (a) Measured Dante radiation temperature history for all shots. (b) Detailed T_R history at the peak

[5] (a) Downscattered proton spectrum for a D^3He-filled capsule showing the shock flash generated protons at 13 MeV and compressional protons centered at 11 MeV. (b) Comparison of proton energy downshift between rugby and cylinder at several viewing orientations.

[6] Measured neutron bang times for all shots. 50 atm DD fill (red), 10 atm DD fill (green), 50 atm D^3He fill (blue). Error bars are ± 50ps for NTD data, ± 100ps for NBT data.

[7] (a) Temporally-gated x-ray emission core images for 50atm DD-filled and 50atm D^3He-filled capsules in both rugby and cylindrical hohlraums. Hohlraum orientation is vertical in all images. (b) Summary of normalized second Legendre polynomial coefficients P_2/P_0 for a 10 atm DD (sequence #1, 7), 50 atm DD (#2, 6), and 50atm D^3He-filled (#3, 5) capsules in (rugby, cylindrical) hohlraums.

[8] (a) Summary of measured outer cone (#3) backscattered energy vs. shot sequence. Rugby (red), cylinder (blue). Inset shows the location of the cone 3 FABS beam on each hohlraum wall. (b) Comparison of measured outer cone backscattered power for rugby (red) and cylinder (blue).

[9] Comparison of Hard X-Ray Detector (HXRD) data for channel 4 (E > 80 keV photons) for rugby (red) and cylinder (blue). Absolute time reference is arbitrary.

[10] (a) Comparison of measured Dante data (shot #54736) vs. simulated Dante histories from simulations including no backscatter (red), measured cone 3 backscatter only (green), measured cone 3 + an additional 5% (blue), 10% (purple), 15% (magenta), and 20% (black) assumed backscatter loss on both inner cones. (b) Comparison of simulated Dante histories between rugby (red) and cylinder (black). Simulations without backscatter are shown with dashed curves and simulations with backscatter losses are shown with solid curves.

[11] Comparison of measured (shot #54736, 50 atm DD-filled rugby) and simulated x-ray bang times vs. level of assumed inner cone backscatter.

[12] Simulated x-ray core emission images with (a) no backscatter, (b) measured cone 3 backscatter only, measured cone 3 + an additional 5% (c), 10% (d), 15% (e), and 20% (f) assumed backscatter loss on both inner cones. (g) Comparison between measurement and simulation of normalized second Legendre polynomial coefficient P_2 / P0 vs. level of assumed inner cone backscatter.

[13] Simulated downscattered proton spectra vs. level of assumed inner cone backscatter at the pole (black) and equator (red).

[14] (a) Comparison of measured (shot # 54739, D^3He-filled, rugby) vs. simulated proton spectra vs. level of assumed inner cone backscatter. Energy downshift of shock flash protons (green), compressional protons in rugby (blue), and compressional protons in cylinder (red). (b) Comparison of simulation vs. data. Blue star is rugby simulation with 15% assumed inner cone backscatter. Red star includes 1.3% backscatter on all cones.

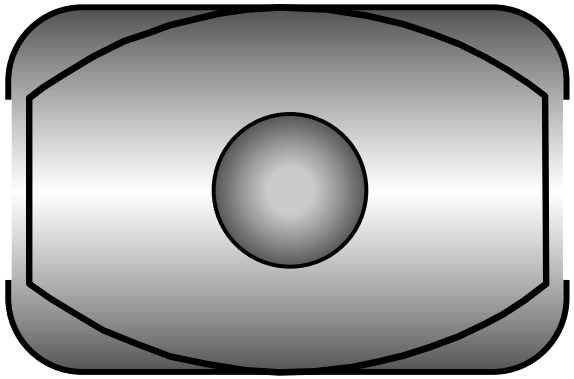

Figure 1

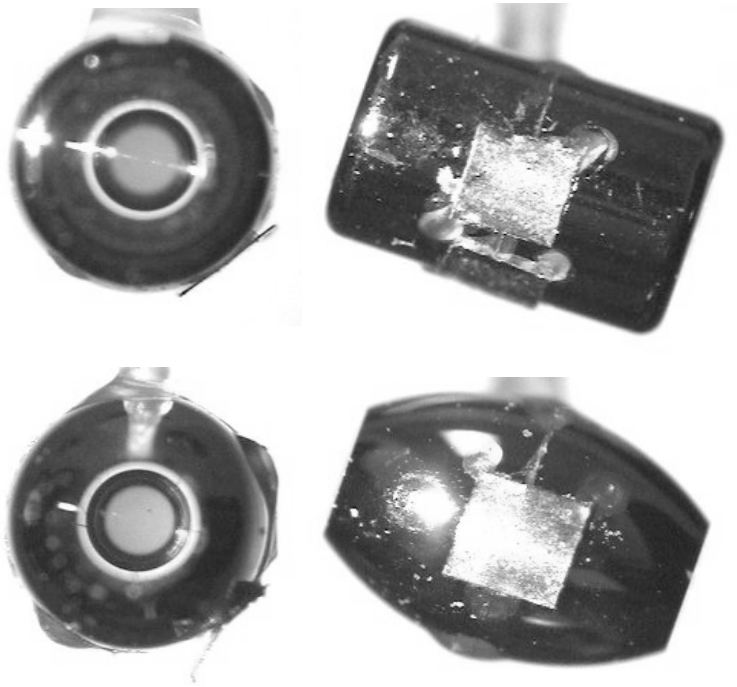

Figure 2

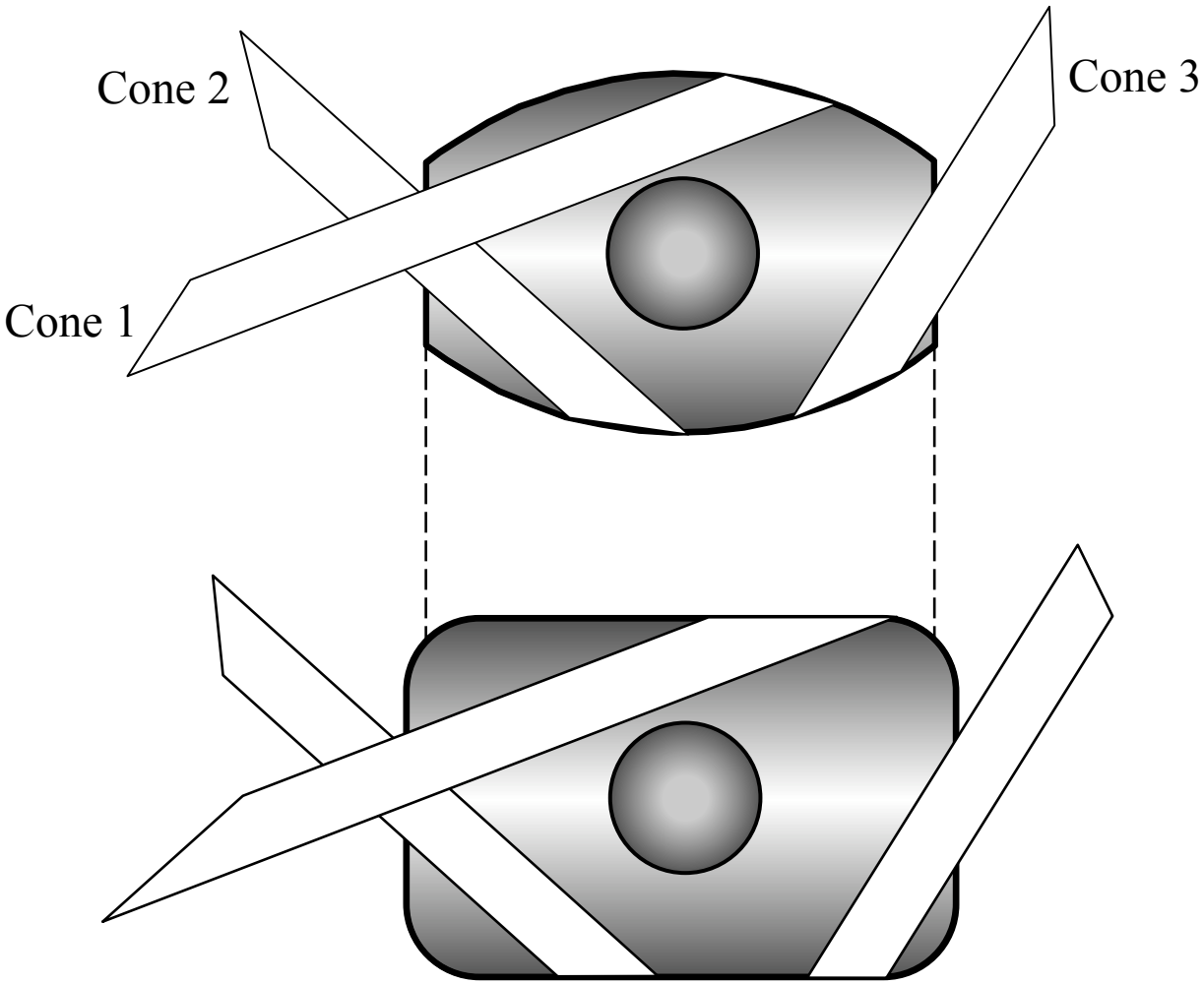

Figure 3

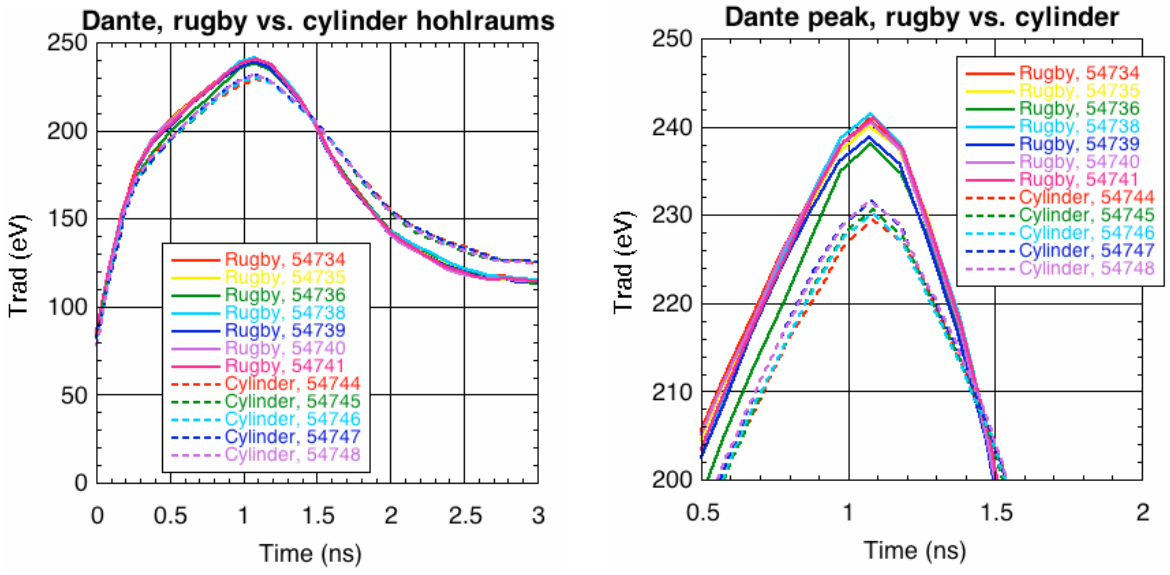
Dante, rugby vs. cylinder hohlraums
Trad (eV)
Time (ns)
Rugby, 54734
Rugby, 54735
Rugby, 54736
Rugby, 54738
Rugby, 54739
Rugby, 54740
Rugby, 54741
Cylinder, 54744
Cylinder, 54745
Cylinder, 54746
Cylinder, 54747
Cylinder, 54748
Dante peak, rugby vs. cylinder
Trad (eV)
Time (ns)
Rugby, 54734
Rugby, 54735
Rugby, 54736
Rugby, 54738
Rugby, 54739
Rugby, 54740
Rugby, 54741
Cylinder, 54744
Cylinder, 54745
Cylinder, 54746
Cylinder, 54747
Cylinder, 54748

Figure 4

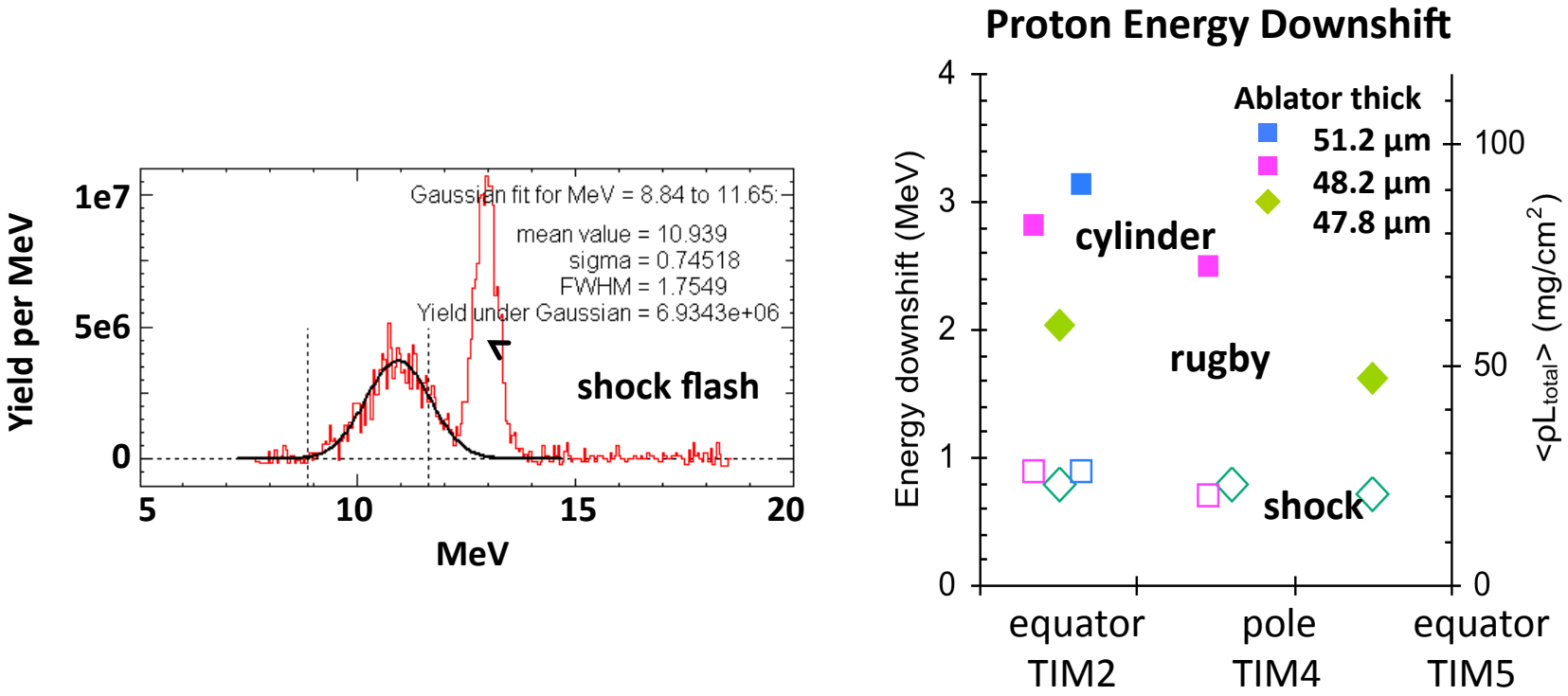
Gaussian fit for MeV = 8.84 to 11.65:
mean value = 10.939
sigma = 0.74518
FWHM = 1.7549
Yield under Gaussian = 6.9343e+06
shock flash
Yield per MeV
1e7
5e6
0
5
10
15
20
MeV
Proton Energy Downshift
Ablator thick
51.2 µm
48.2 µm
47.8 µm
cylinder
rugby
shock
Energy downshift (MeV)
<pL_total> (mg/cm^2)
4
3
2
1
0
100
50
0
equator
TIM2
pole
TIM4
equator
TIM5

Figure 5

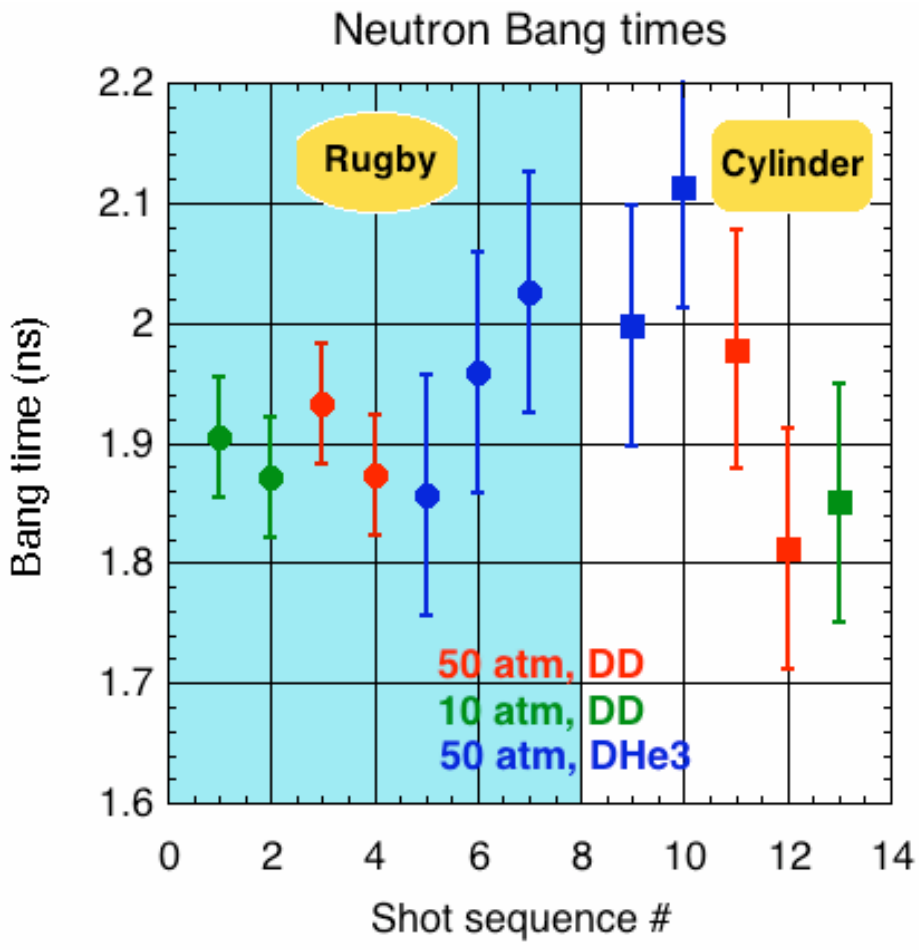
Neutron Bang times
Rugby
Cylinder
50 atm, DD
10 atm, DD
50 atm, DHe3
Bang time (ns)
Shot sequence #
2.2
2.1
2
1.9
1.8
1.7
1.6
0
2
4
6
8
10
12
14

Figure 6

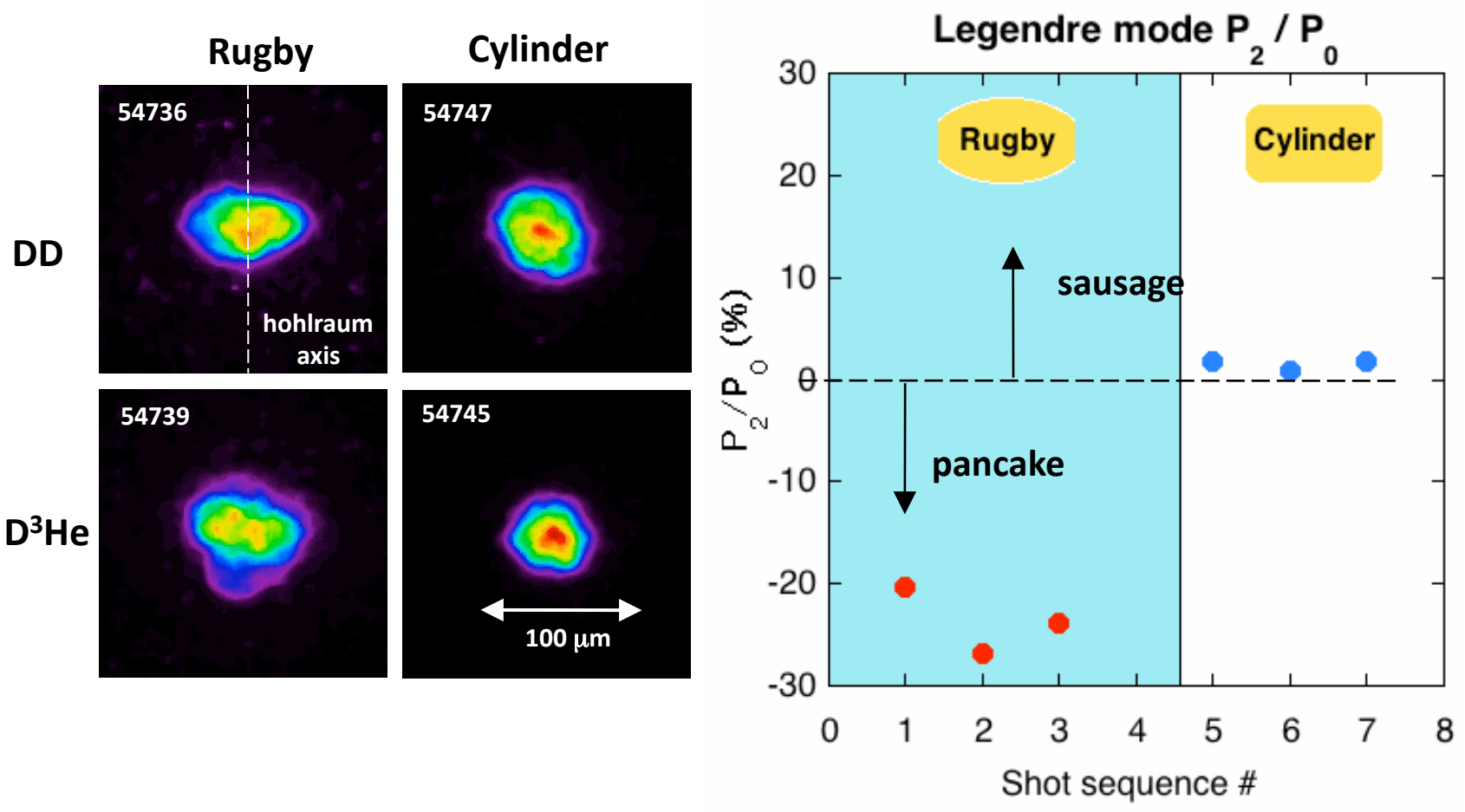
Rugby
Cylinder
DD
D3He
54736
54747
54739
54745
hohlraum axis
100 μm
Legendre mode P2 / P0
Rugby
Cylinder
sausage
pancake
P2/P0 (%)
Shot sequence #
30
20
10
0
-10
-20
-30
0
1
2
3
4
5
6
7
8

Figure 7

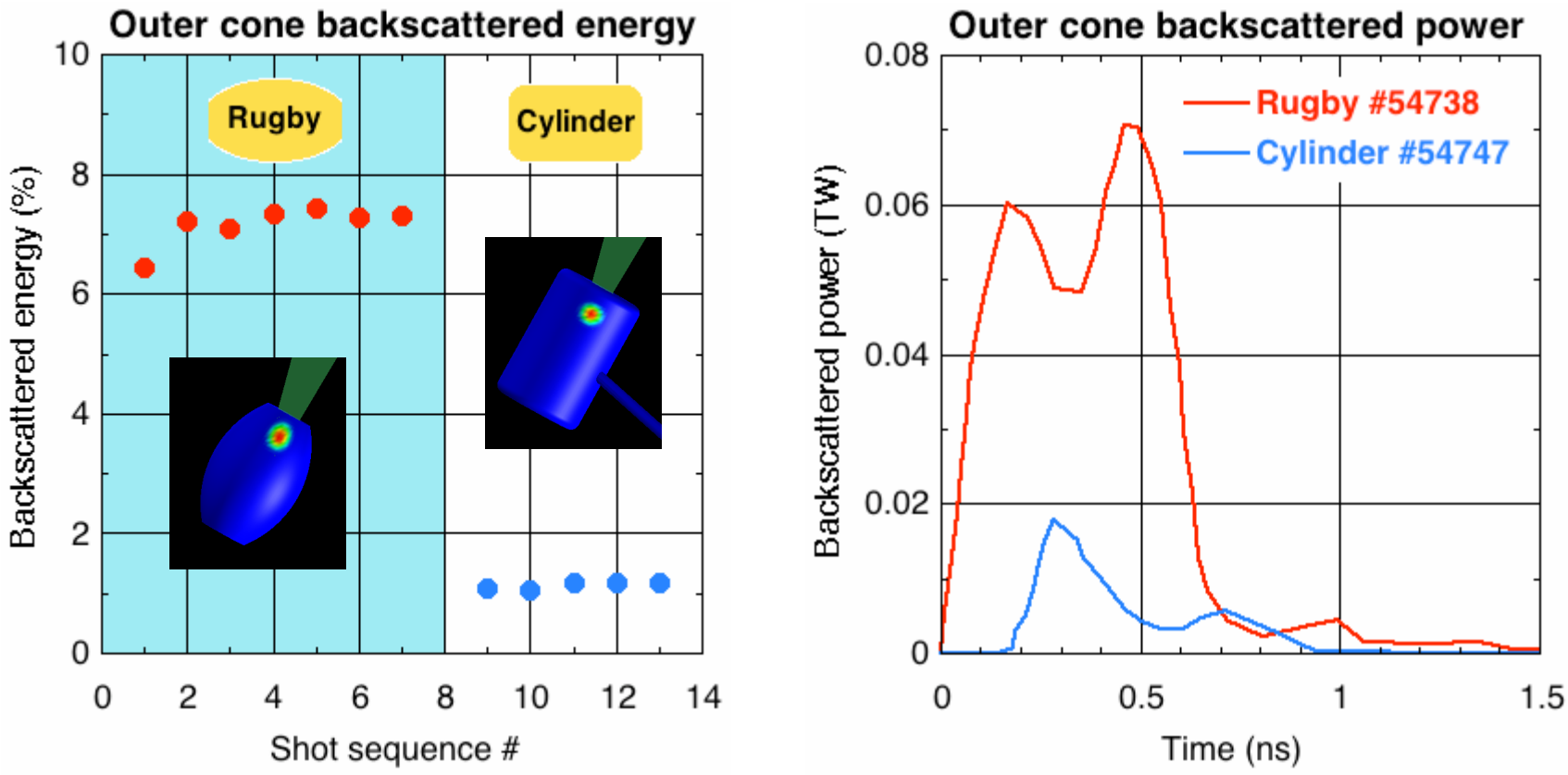
Outer cone backscattered energy
Rugby
Cylinder
Backscattered energy (%)
Shot sequence #
0
2
4
6
8
10
12
14
Outer cone backscattered power
Rugby #54738
Cylinder #54747
Backscattered power (TW)
Time (ns)
0.08
0.06
0.04
0.02
0
0.5
1
1.5

Figure 8

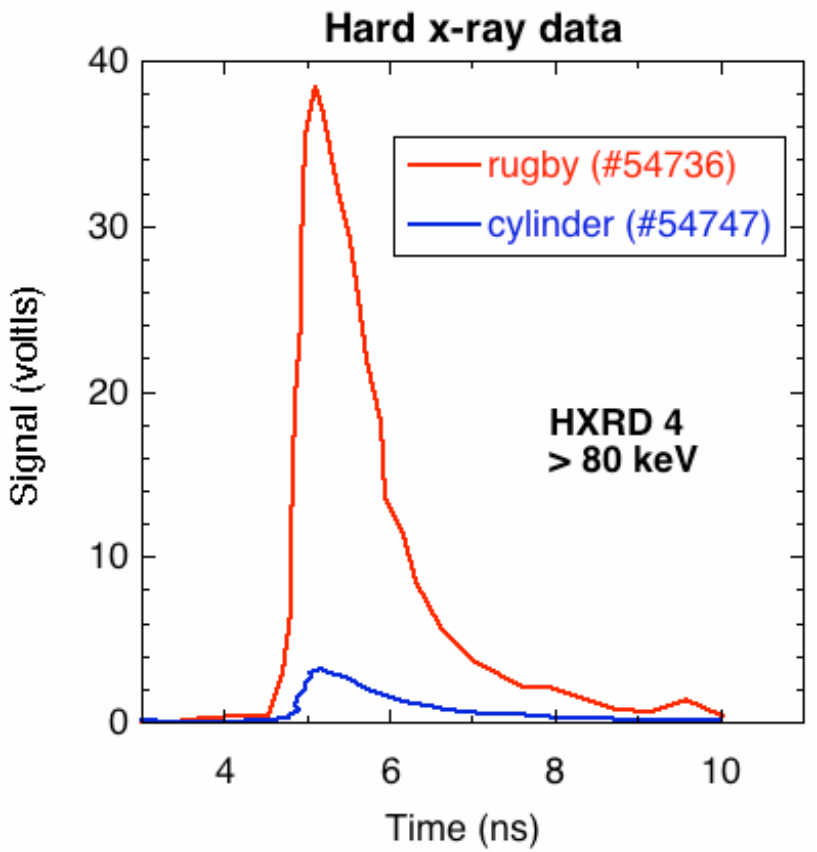
Hard x-ray data
rugby (#54736)
cylinder (#54747)
HXRD 4
> 80 keV
Signal (volts)
Time (ns)
0
10
20
30
40
4
6
8
10

Figure 9

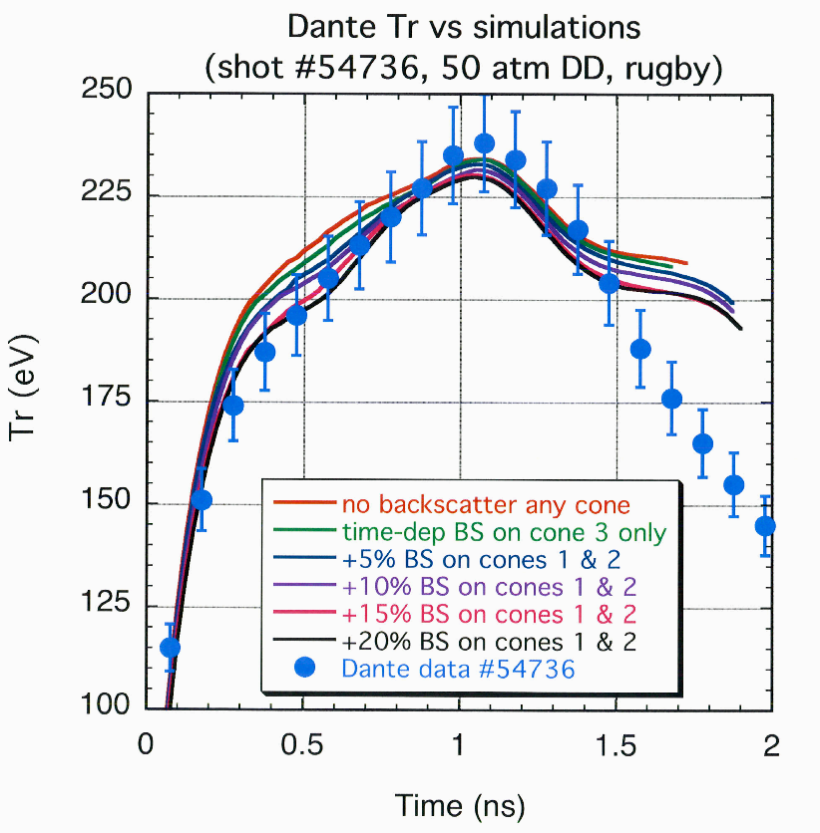
Dante Tr vs simulations
(shot #54736, 50 atm DD, rugby)
Tr (eV)
Time (ns)
250
225
200
175
150
125
100
0
0.5
1
1.5
2
no backscatter any cone
time-dep BS on cone 3 only
+5% BS on cones 1 & 2
+10% BS on cones 1 & 2
+15% BS on cones 1 & 2
+20% BS on cones 1 & 2
Dante data #54736

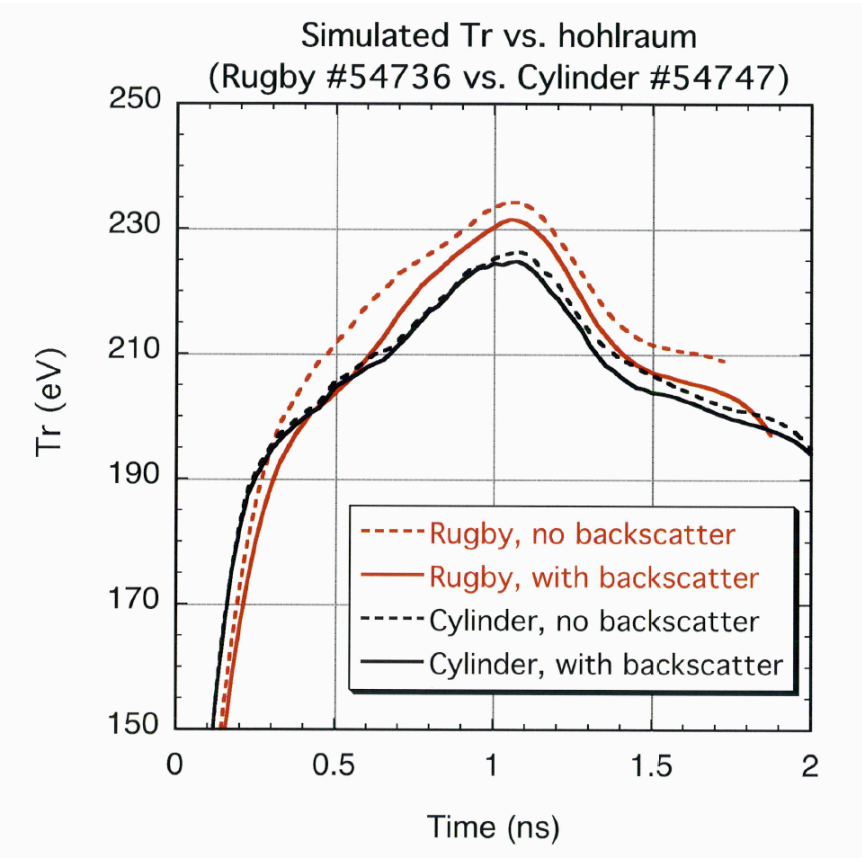
Simulated Tr vs. hohlraum
(Rugby #54736 vs. Cylinder #54747)
Tr (eV)
Time (ns)
250
230
210
190
170
150
0
0.5
1
1.5
2
Rugby, no backscatter
Rugby, with backscatter
Cylinder, no backscatter
Cylinder, with backscatter

Figure 10

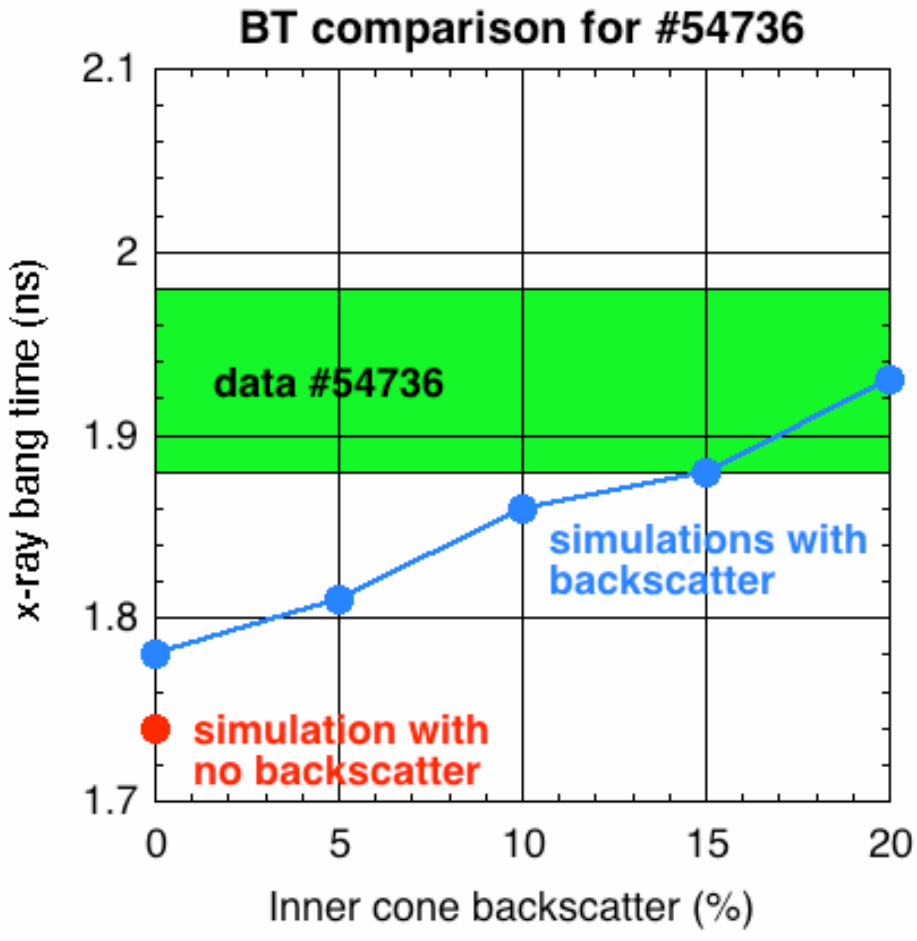
BT comparison for #54736
2.1
2
1.9
1.8
1.7
x-ray bang time (ns)
data #54736
simulations with
backscatter
simulation with
no backscatter
0
5
10
15
20
Inner cone backscatter (%)

Figure 11

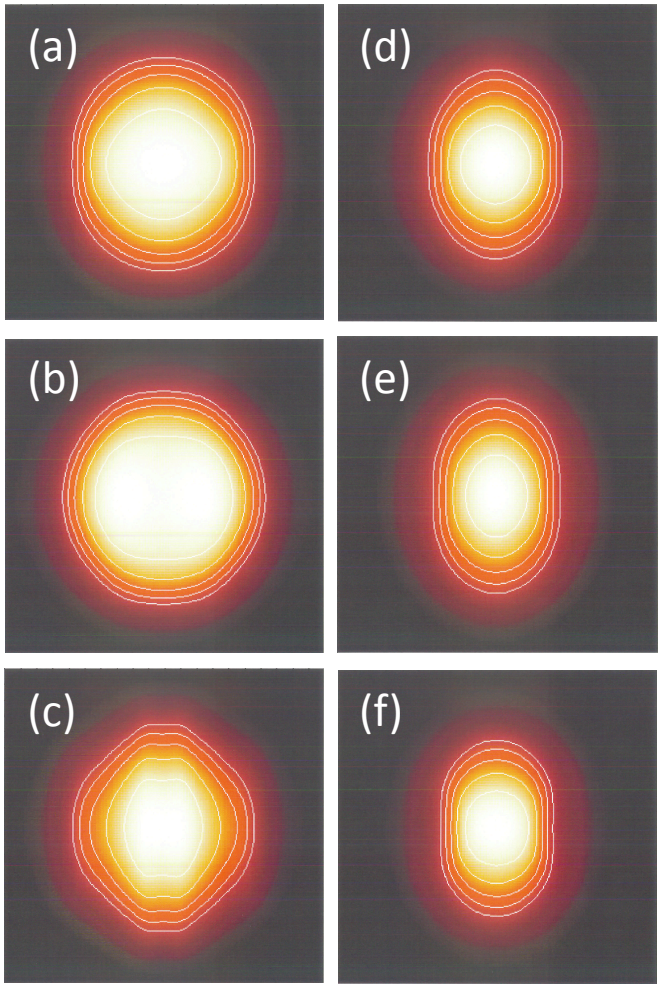
(a)
(d)
(b)
(e)
(c)
(f)

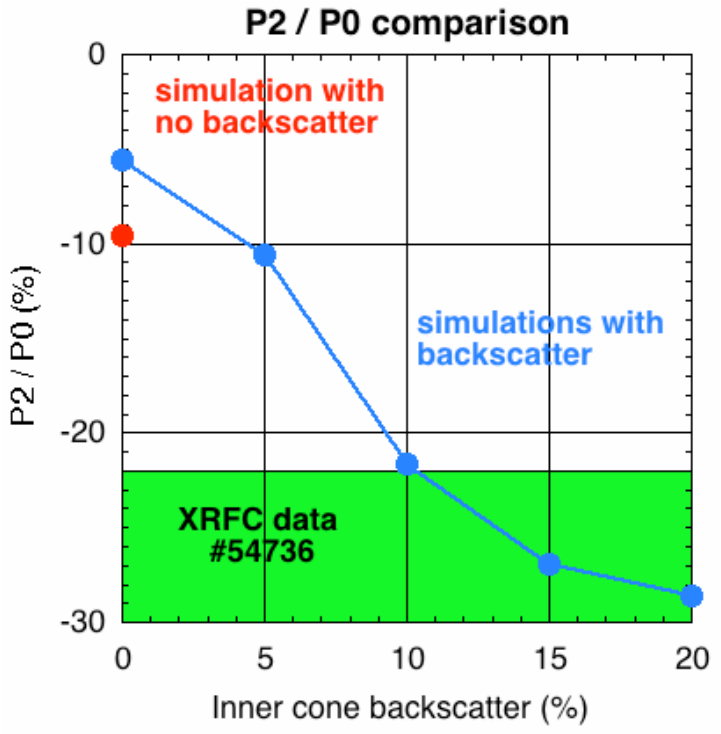
P2 / P0 comparison
simulation with
no backscatter
simulations with
backscatter
XRFC data
#54736
P2 / P0 (%)
0
-10
-20
-30
0
5
10
15
20
Inner cone backscatter (%)

Figure 12

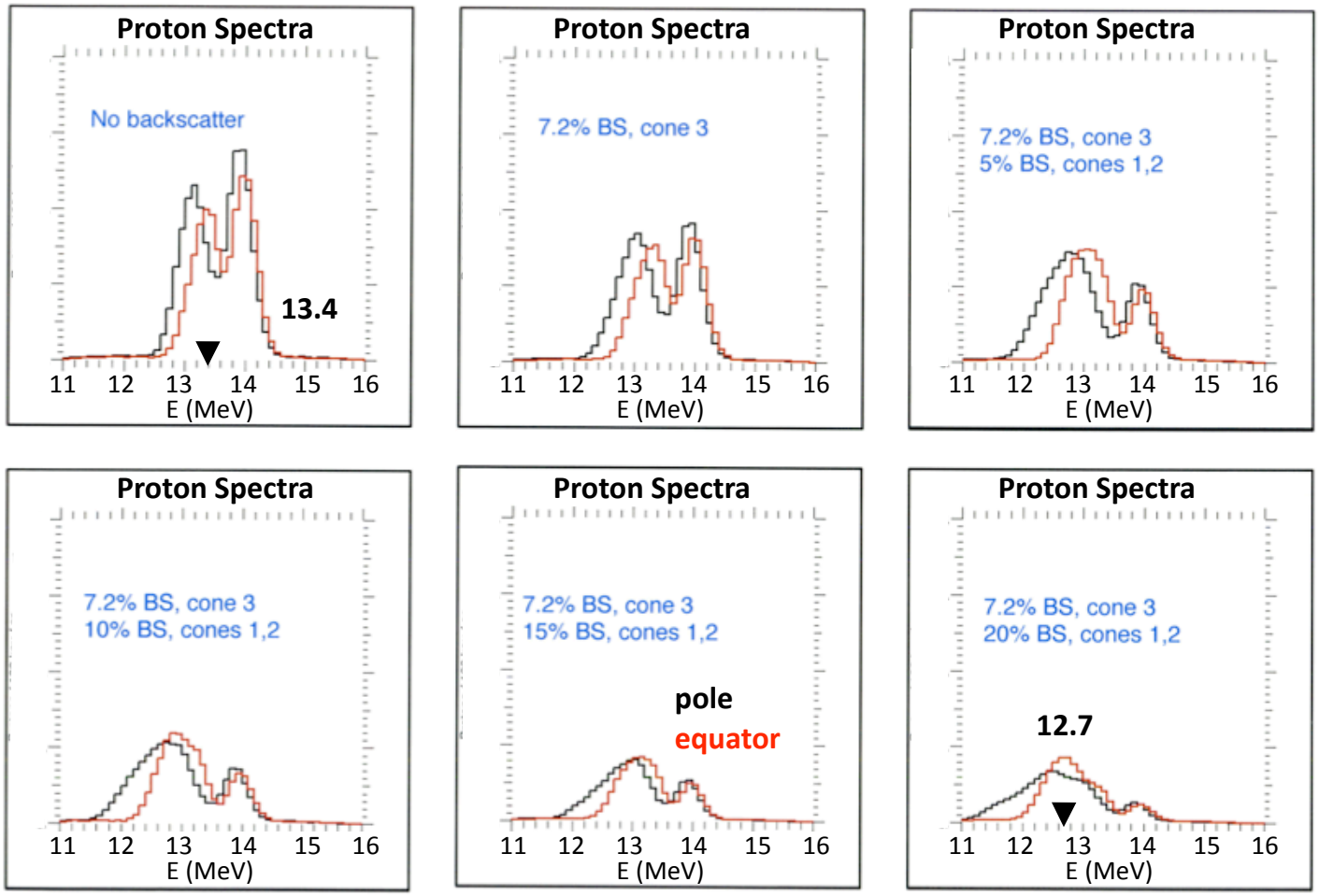
Proton Spectra
No backscatter
13.4
11 12 13 14 15 16
E (MeV)
Proton Spectra
7.2% BS, cone 3
11 12 13 14 15 16
E (MeV)
Proton Spectra
7.2% BS, cone 3
5% BS, cones 1,2
11 12 13 14 15 16
E (MeV)
Proton Spectra
7.2% BS, cone 3
10% BS, cones 1,2
11 12 13 14 15 16
E (MeV)
Proton Spectra
7.2% BS, cone 3
15% BS, cones 1,2
pole
equator
11 12 13 14 15 16
E (MeV)
Proton Spectra
7.2% BS, cone 3
20% BS, cones 1,2
12.7
11 12 13 14 15 16
E (MeV)

Figure 13

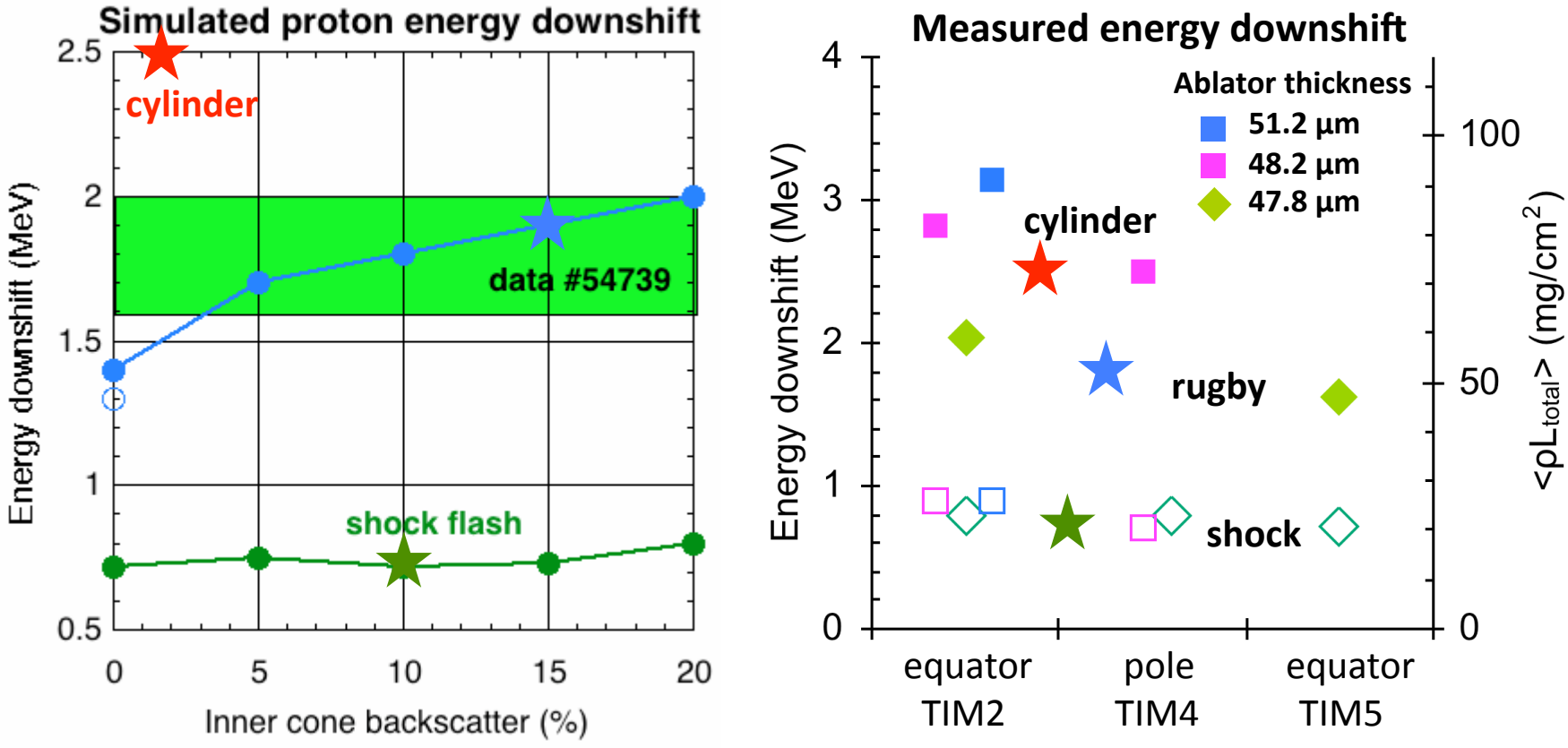
Simulated proton energy downshift
cylinder
data #54739
shock flash
Energy downshift (MeV)
Inner cone backscatter (%)
2.5
2
1.5
1
0.5
0
5
10
15
20
Measured energy downshift
Ablator thickness
51.2 µm
48.2 µm
47.8 µm
cylinder
rugby
shock
Energy downshift (MeV)
<ρL_total> (mg/cm²)
4
3
2
1
0
100
50
0
equator
TIM2
pole
TIM4
equator
TIM5

Figure 14